Journal of Materials Chemistry A

Contribution of BN-co-doped Reduced Graphene Oxide as a Catalyst Support on Activity of Iridium Oxide for Oxygen Evolution Reaction

Journal:	*Journal of Materials Chemistry A*
Manuscript ID	TA-ART-01-2021-000158.R1
Article Type:	Paper
Date Submitted by the Author:	02-Mar-2021
Complete List of Authors:	Joshi, Prerna; Toyota Technological Institute, Graduate School of Engineering Yadav, Rohit; Toyota Technological Institute, School of Engineering Hara, Masanori; Toyota Technological Institute, Graduate School of Engineering Inoue, Tetsunari ; Toyota Technological Institute, Catalytic Organic Chemistry Laboratory Motoyama, Yukihiro; Toyota Technological Institute, Catalytic Organic Chemistry Laboratory Yoshimura, Masamichi; Toyota Jidosha Kabushiki Kaisha,

ARTICLE

Contribution of BN-co-doped Reduced Graphene Oxide as a Catalyst Support on Activity of Iridium Oxide for Oxygen Evolution Reaction

Received 00th January 20xx
Accepted 00th January 20xx

DOI: 10.1039/x0xx00000x

Prerna Joshi[a*], Rohit Yadav[a], Masanori Hara[a], Tetsunari Inoue[b], Yukihiro Motoyama[b], Masamichi Yoshimura[a]

The current research deals with the study of boron and nitrogen co-doped reduced graphene oxide (BN-rGO) as a support material for iridium oxide (IrO_2) nanoparticles for oxygen evolution reaction (OER) catalysis. The synthetic approach for IrO_2-BN-rGO catalyst involves the combination of pyrolysis and hydrothermal method used for hierarchical nanostructures. BN-rGO possesses B-N, B-C, and N-C functional groups to support and stabilize the IrO_2 catalyst nanoparticles. The altered electronic states of IrO_2 on BN-rGO support are compared with IrO_2 on a non-doped support, rGO (IrO_2-rGO) and on commercial BN sheets (IrO_2-c-BN). The catalyst shows low overpotential (300 mV at 10 mA cm^{-2}), high current density (55 mA cm^{-2} at 1.65 V), and significantly high durability (12350 cycles; 45 h) in an acidic environment. The high stability of IrO_2-BN-rGO may come from the presence of a chemically and electrochemically stable B-N bond. We confirm that other functional groups (B-C, N-C) and rGO framework are equally crucial for the better attachment of IrO_2 nanoparticles.

Introduction

In the present scenario of increasing energy demand and depleting energy resources, hydrogen evolution from water splitting is the environment-friendliest alternative to meet the current energy requirements. However, slow reaction kinetics and high overpotentials (η), required for oxygen evolution reaction (OER) at anode, constraint its practical application. In recent years, considerable developments on highly active and durable OER electrocatalysts have been reported, majorly involving noble metals and metal oxides such as Ir, Ru, RuO_2, IrO_2, which show better performance in acidic solutions,[1] but their high cost and scarce resources limit their commercialization. Among these, IrO_2 has been reported to show 60 and 30 times higher stability than Ir metal and RuO_2, respectively.[2] Apart from these noble metals, certain inexpensive alternatives, such as transition metal oxides (TMOs), e.g. MnO_2,[3] Co_2O_3,[4] NiCoO,[5] and carbon materials like carbon nanotubes (CNTs),[6] carbon dots,[7] and graphene[8] have shown OER activity in both acidic and alkaline environments. To work hand in hand with the hydrogen evolution reaction (HER) catalysts in acidic environments,[9,10] electrode material with improved activity, durability and electrical conductivity is required. Poor electronic conductivity of TMOs and easier corrosion of carbon-based catalysts limit the utilization of such single-component materials[11] for OER in acidic medium. Therefore, composite materials with synergistic effect of combined properties of individual components, and their interactions,[11] come into picture. In this regard, metal-oxide nanoparticles (nps) decorated on highly conductive supports are potential OER catalysts.[1,12] Both experimental and theoretical investigations have proven that conductive supports such as doped graphene can modify the electronic states of the supported metal catalysts because of their high electrical conductivity,[13,14] making them useful in the field of electrocatalysis.

Commonly known, nitrogen-[15] and boron-doped graphene[16] have been reported as excellent catalysts for oxygen reduction reaction (ORR) and OER, as well as supports for metal oxide catalysts for OER.[17,18] The B-C and N-C functionalities in doped graphene produce extra electronic states[19] of the supported metal catalysts and modify them because of the stronger metal-support interaction (SMSI). In this regard, dual atom or biatomic doping (B and N co-doping) of carbon materials has also been widely reported because of the distinct electronic structure, arising from synergistic coupling of the three atoms, B (2.04), C (2.55) and N (3.04) with different electronegativities.[20] Heteroatom doping in graphene enhances the electrical conductivity of the graphene framework by induction of a small band gap and p- or n-type conductivity. With B or N doping in graphene, two distinct phenomena follow, **i)** the band gap decreases with increasing B or N concentration and **ii)** the finite density of states (D) at zero energy in the density of states of graphene *appear*, due to increased quasiparticle weight because of the presence of heteroatom, in contrast to the pure graphene case where D completely *vanishes*.[21] The appearance

[a]*Surface Science Laboratory, Toyota Technological Institute, Nagoya 468-8511, Japan*
[b]*Catalytic Organic Chemistry Laboratory, Toyota Technological Institute, Nagoya 468-8511, Japan*
Electronic Supplementary Information (ESI) available: See DOI: 10.1039/x0xx00000x

of allowed states occurs close to zero energy but at shifted Fermi level. The two events participate in increasing the electrical conductivity with increased B or N doping.[21] B-doped reduced graphene oxide (rGO) with B-C bonds and a few O-functional groups has been reported to show the electrical conductivity of 44 Scm^{-1} which is higher than that of rGO (1.81 Scm^{-1}).[22] For N-doped graphene (NG), the electrical conductivity with pyridinic N is reported to be 0.92-0.06 x 10^3 Sm^{-1}.[23] Interestingly, for a B, N co-doped graphene, the electronic conductivity greatly depends on the presence of BN clusters or individual distribution of B and N functional groups. Based on both theoretical and experimental results, Wang *et al.* reported that **a)** low carbon content on BN co-doped graphene (BNG) leads to poor electronic conduction, **b)** presence of a large BN cluster also disrupts the catalytic activity of BNG due to the highly insulating nature of BN bonds, yet **c)** even in the presence of a few BN bonds, electronic conduction can occur in graphene influencing its electronic properties.[24]

If we focus on the structure of the heteroatoms in the catalyst, the B and N functionalities can be categorized into two main groups, i.e. **a)** B and N bonded separately to a C atom (B-C/N-C groups) and **b)** B and N bonded to each other (B-N pair). Distinctively, both these groups exhibit contrasting behaviour. The formation of separate B-C and N-C functional groups tends to activate the carbon π-system which is *beneficial* for chemisorption of oxygen for ORR.[25] In a contradictory manner, the presence of B-N pair *hinders* the rate of O_2 adsorption on nano-carbon surface.[26] Therefore, BNG with negligible B-N pair content are suitable ORR electrocatalysts.[20] On the other hand, theoretical calculations show that depending on the co-dopant bond arrangements in graphene, the electrochemical properties change. Schiros *et al.* reported a DFT study on B-N dopant structures in single layer graphene.[27] According to their study, depending on the B: N ratio, it is possible to create p- and n-type domains in a single carbon sheet which can open a gap between valence and conduction bands in graphene (no gap for B: N=1:1). The comparable electron withdrawing and electron donating effects participate in altering the work function of graphene, which activates the material for several electrochemical and optical applications.[28] In consistence with this, several literatures reported the use of carbon doped boron nitride (BN) sheets as support for Ir-oxide catalysts towards oxygen electrocatalysis. Liu *et al.* reported the use of laser-modified B, N nanospheres with C, O doping as excellent catalyst support for OER, stating that doping C into BN can form C-N/C=N bonds to enhance the interaction between the support and the catalyst.[29] 3D fluffy PtPd nanocorals decorated on 2D hexagonal BN supports were reported to show long-term durability in alkaline medium towards methanol and ethanol oxidation reactions in fuel cells.[30] BNG has also been studied as a support material for various energy conversion processes, such as hydrazine dehydrogenation, methanol[31] and ethanol oxidation in direct ethanol fuel cells,[32] and polyaniline-based electric double layer capacitor.[33] These literatures (summarized in **Table S1**) offer a possibility of a similar restructuring in nano-carbon material with a B-N pair so as to obtain high activity and

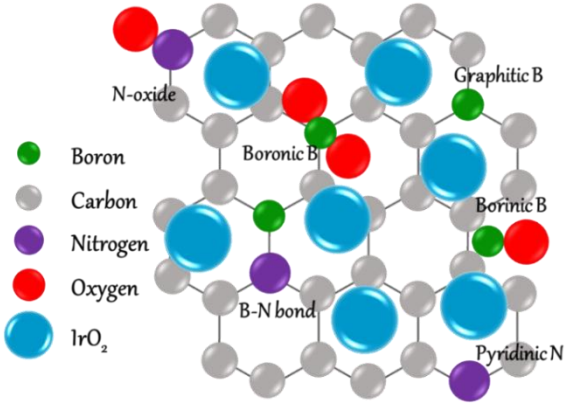

Figure 1 Pictorial representation of IrO_2 nps deposited on BN-rGO sheets, along with the probable functional groups. The depiction of the coloured dots is provided in the inset.

improved stability for BN-based carbon materials as supports in electrolysis. To our advantage, the use of BNG supported IrO_2 nps as OER catalyst has not been reported. The experimental evidence of the advantage of B-N pair in terms of localized active sites with improved chemical and electrochemical stability in acidic medium, has scarcely been discussed.

In this article, we study the effect of boron and nitrogen co-doped reduced graphene oxide (BN-rGO) as a catalyst support for OER in acidic solution. BN-rGO support is synthesized by pyrolysis of graphene oxide (GO) with urea and boron anhydride, followed by hydrothermal reaction to deposit IrO_2 nps. BN-rGO, synthesized in such a manner, is expected to possess B-C and N-C functional groups on rGO with altered electronic states of deposited IrO_2 nps (**Figure 1**). The catalytic activity and durability of IrO_2-BN-rGO is examined in acidic medium and the change in morphology and electronic states after the durability test is analysed by TEM and XPS. The changes in morphology and formation of adsorbed intermediates during the durability test are supported by gradual variation in Tafel slope. We further compare our results with IrO_2 supported on non-doped rGO (IrO_2-rGO), and highlight the importance of a conductive 2D-rGO framework in improving the OER performance in acidic medium. To the best of our knowledge, this is the first report on the contribution of BN-co-doped rGO support towards improving the OER performance of IrO_2.

Experimental

Materials and methods

The catalyst, IrO_2-BN-rGO, was synthesized by a similar procedure as described in our reported work.[17,18] Briefly, graphene oxide (GO), synthesized by modified Hummers' method,[34] urea (CON_2H_4, Kishida Chemical Co.) and boron anhydride (B_2O_3, BA, Sigma Aldrich) were mixed in weight ratio of GO: Urea: BA=1:5:5 to obtain equal B and N doping content. The mixture was ultrasonicated at room temperature (r.t.) for 60 min, and freeze dried for 24 h, followed by pyrolysis in a tube furnace at 1000 °C for 60 min in N_2 atmosphere to obtain BN-rGO as the support. Dihydrogen hexachloroiridate (H_2IrCl_6) and

BN-rGO were mixed together in ethanol: water (9:1) solution and the mixture was ultrasonicated for 1 h followed by stirring for 2 h. The obtained mixture was refluxed for 6 h at 80 °C and transferred to a Teflon-lined autoclave for hydrothermal synthesis at 150 °C for 4 h to obtain IrO_2 nps deposited on BN-rGO (IrO_2-BN-rGO). The final product was washed with ethanol: water (9:1) and dried in vacuum for 6 h at 80 °C. We further compared our results with that of non-doped rGO as support (IrO_2-rGO), synthesized in a similar manner. Since, there is a possibility of B-N bond formation due to the annealing of B and N together at high temperature, we also decorated IrO_2 nps on commercial BN (c-BN, flake size <1 μm, Sigma Aldrich) via hydrothermal method (IrO_2-c-BN) under the same condition of IrO_2-BN-rGO synthesis, to confirm the chemical composition of our catalyst. Following the IUPAC nomenclature,[35,36] the supports and the catalysts are named as $B_{9.4}CN_{11.5}$, $B_{27.2}N_{37.6}$, IrO_2-C, IrO_2-$B_{9.4}CN_{11.5}$ and IrO_2-$B_{27.2}N_{37.6}$, however, in the present article, we have used the common names for the catalysts as BN-rGO, c-BN, IrO_2-rGO, IrO_2-BN-rGO and IrO_2-c-BN, respectively.

The distribution of IrO_2 nps and the particle diameter were analysed by transmission electron microscopy (TEM, TEM-2100, JEOL, operated at 120 kV). The nanoparticle (np) surface area of the deposited IrO_2 nps was calculated using TEM, considering the density of IrO_2 equal to 11.66 g cm^{-3}.[37] Further, morphology of GO, rGO, BN-rGO, c-BN, IrO_2-rGO, IrO_2-BN-rGO and IrO_2-c-BN was studied by scanning electron microscopy (SEM, SU3500, Hitachi High Technologies Co., operated at 15 kV) equipped with an energy dispersive X ray spectrometer (EDX, EMAX Evolution X-Max, Horiba Ltd., operated at 15 kV). Microwave plasma atomic emission spectrometry (MP-AES, Agilent 4200 MP-AES Spectrometer) analysis was done to confirm the amount of Ir in the catalysts. For MP-AES, optimum amount of catalyst was dissolved in aqua-regia for 112 h and further, heated at 150 °C for 12 h. The undissolved remnants were removed by filtration using membrane filters (Durapure®; 0.45 mm HV) followed by optimum dilution in using 1N HCl (Wako Chemicals). The Ir contents were calibrated with a standard solution (Kanto Kagaku, 1 mg/mL Ir, 20 % HCl). Raman spectroscopy (In-Via Renishaw Microscope, 532 nm laser source) was employed to study the reduction of GO, degree of defects induced due to BN-doping in GO, and difference in structure between BN-rGO and c-BN. The crystallinity of the synthesized catalysts was studied by X-ray diffraction analysis (Ultima 4, Rigaku Co.) with Cu Kα (0.15405 nm). The *d* spacing, distance between the adjacent GO sheets or layers, was calculated by the Bragg's law, $d = \lambda / (2 \sin(\theta))$, where λ is the wavelength of the X-ray beam (Cu Kα = 0.154 nm).[38] The elemental composition, amount of functional groups in GO, and type of B, N functionalities and Ir in IrO_2-BN-rGO were analysed by X-ray photoelectron spectroscopy (XPS, PHI5000 Versa Probe II, ULVAC-PHI) with Al Kα radiation (1486.6 eV) anode.

The OER catalytic activities of the synthesized catalysts were measured by linear sweep voltammetry (LSV) using HSV-110 potentiostat (Hokuto Denko Co.) with rotating disk electrode (RDE) equipment (RRDE-3A, BAS Inc.) at r.t. (23 ± 2 °C) in the potential range of 1.20 to 1.65 V vs. RHE at the scan rate of 5 mV s^{-1} in 0.5 M H_2SO_4 solution. Pt wire, Ag/AgCl in 3 M KCl and IrO_2-BN-rGO were used as the counter electrode, reference electrode, and working electrode (WE), respectively. WE was prepared using the catalyst ink composed of synthesized catalyst dispersed in distilled water (DI), isopropylalcohol (IPA, Tokyo chemicals Ltd.) and Nafion (added 5 wt.% of the catalyst, Sigma Aldrich) by ultrasonication for 30 min. Aliquot of the catalyst ink was dropped on alumina (0.05 μm) polished glassy carbon electrode (GC, 3 mm in diameter, geometrical area of the electrode = 0.07 cm^2) and spin-coated at 400 rpm. The coated electrode was dried at atmospheric pressure for 24 h at r.t. Ir metal amount on each electrode was kept same (140 μg cm^{-2}). All the potentials in the article are reported with respect to reversible hydrogen electrode (RHE) unless otherwise stated, calculated using the equation, $E_{(vs\ RHE)} = E_{(vs\ Ag/AgCl)} + 0.059\ pH + E^o_{(Ag/AgCl)}$, where $E^o_{(Ag/AgCl)} = 0.210$ V and pH (0.5 M H_2SO_4) = 0.38.[39] Before the analysis, the electrolyte solution was purged with N_2 continuously at an optimum rate for 40 min to obtain a N_2 saturated electrolyte solution. Further, during the electrochemical measurements, a gentle N_2 flow was maintained over the solution. Ultrapure water (18.2 MΩ cm) was used for preparation of all the catalysts and electrochemical measurements. Accelerated durability tests (ADT) were carried out to test the durability of the catalyst where the catalyst was cycled for *n* number of cycles between 1.0 to 1.3 V vs RHE at 50 mV s^{-1} in the same electrolyte solution. The Tafel equation ($\eta = a + b \log i$, where $\eta = E - E_o$ (E_o= 1.23 V vs RHE) was used to calculate Tafel slope, *b*, by plotting log *i* vs η in the overpotential region (0.225 V to 0.350 V) for all the samples. The change in morphology of nps and composition of catalysts after ADT were examined by TEM and XPS analysis, respectively.

Results and discussion

Our synthetic approach follows the methodology of designing hierarchical graphene electrocatalysts.[40] Different routes of synthesis of heteroatom-doped graphene based catalysts are present in literature that emphasize on the electronic behaviour of the graphene support using heteroatom doping. Wang *et al.* reported the synthesis of BN co-doped vertically aligned carbon nano-tubes (VACNTs) as electrocatalysts for ORR by thermal annealing of GO with B and N precursors leading to tuned levels of BN co-doping in equal amounts, $B_{12}C_{77}N_{11}$.[41] The BCN catalyst exhibited better catalytic activities than conventional Pt/C, due to the creation of smaller band gap caused by the equal amount of biatomic doping. Sequential doping of B and N in graphene was also reported by Zheng *et al.* that claimed the prevention of inactive by-product formation.[42] This catalyst displayed comparable ORR results to that of the Pt/C catalyst. Another innovative method to design hierarchical electrocatalysts was introduced by Di Noto *et al.* as core-shell catalysts where active metal sites supported on a shell (carbon nitride nanoclusters) were decorated on a core (electron-conducting active carbons or metal nanopowders) featuring a well-controlled deposition

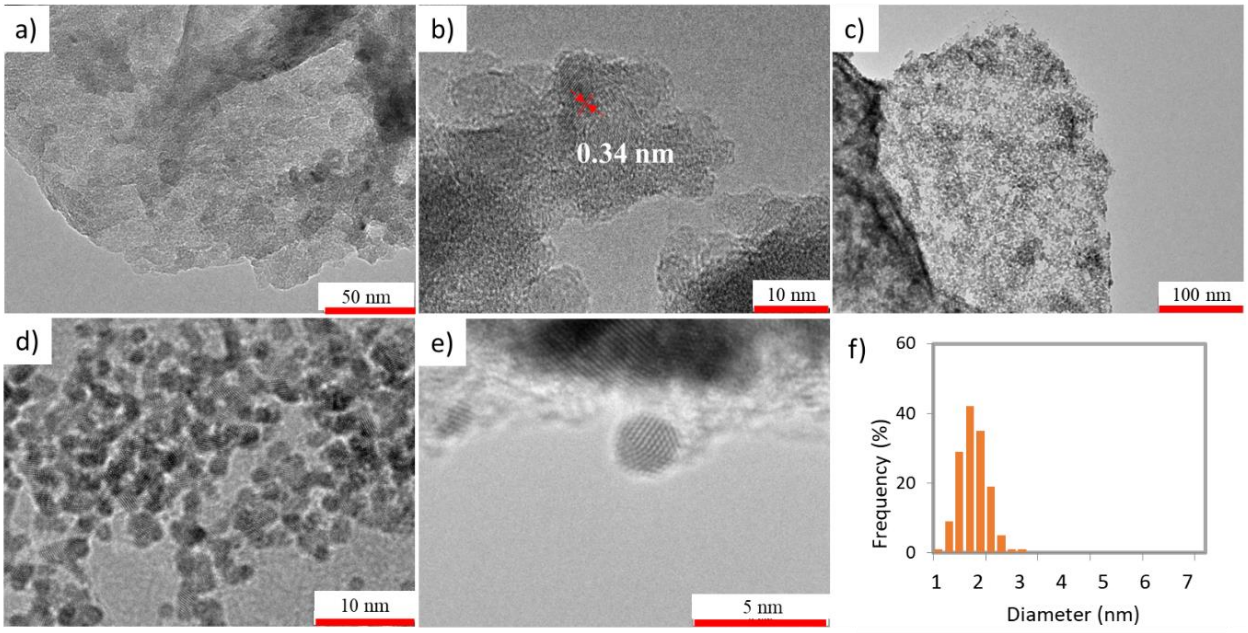

Figure 2 TEM images of **a, b)** BN-rGO sheet, **c, d)** IrO_2-BN-rGO, **e)** high resolution image of IrO_2 np and **f)** particle distribution of IrO_2 nps on BN-rGO.

of the metal catalyst with desired amount of dopant.[43] Impregnation of a polyurethane foam with water suspension of GO sheets and urea is another method to design doped graphene based hierarchical electrocatalyst.[44] In this method, the synthesis is carried out in two steps of calcination at 900°C in an Ar atmosphere and conventional microwave-assisted polyol process to load the Pt nps, yielding the final Pt/3D-NG product. Our synthetic scheme followed a similar methodology where we first design the doped carbon support via pyrolysis in an inert atmosphere and the extent of doping can be altered by controlling the temperature of pyrolysis.[45] The process can be easily scaled up allowing mass production of the BN co-doped support with tuned doping levels. The second step in our synthetic approach is the deposition of metal oxide nps on the doped nano-carbon via hydrothermal method at low temperature (T = 150°C). The amount of reactants can be regulated to control the amount of deposited nps, hence, all three catalysts were obtained to contain Ir in approximately similar amounts (~11.0 - 12.0 wt.%). Moreover, the precise control of temperature, time, and amount of solvent in this process leads to size-controlled nps in the size range of 1.5 – 1.7 nm. The hydrothermal treatment triggers the formation of the nps with controlled particle size and also contributes to the reduction of unreduced GO.

Morphological Characterization. The homogeneous decoration of IrO_2 nps on BN-rGO sheets was confirmed by TEM analysis. **Figure 2** shows the TEM images of BN-rGO sheet (**Figure 2a, b**), IrO_2-BN-rGO (**Figure 2c-e**) and its particle size distribution (**Figure 2f**). rGO (**Figure S1b**) and BN-rGO were found to be sheet-like wrinkled structure, which is a characteristic feature of reduced GO sheets. The lattice spacing in BN-rGO was estimated to be 0.34 ± 0.01 nm, which is in correspondence with that observed from XRD (**Figure 3b**), as described below. The value of lattice spacing for BN-rGO sheets was in between that of rGO sheets (0.36 ± 0.02 nm) **(Figure S1b)** and c-BN (0.32 ± 0.03 nm) (**Figure S1c**) implying the shrinking of rGO structure after biatomic doping. The uniform distribution of IrO_2 nps on BN-rGO was also confirmed by TEM (**Figure 2 c-f**) and the average particle diameter for IrO_2 nps was estimated to be 1.7 ± 0.1 nm. Furthermore, the high resolution image of IrO_2 np in **Figure 2e** shows the lattice spacing for IrO_2 nps to be ca. 0.23 ± 0.02 nm which is consistent with that of the (200) plane of IrO_2 reported in our previous work.[17] The IrO_2 nps decorated on rGO lattice (**Figure S2 a, b, c**) and c-BN (**Figure S2 d, e, f**) showed the average np diameter of 1.5 ± 0.4 and 1.6 ± 0.3 nm, respectively. The calculated particle size (nm) and mean spacing (nm) of the designed IrO_2 catalysts are listed in **Table 1**. Successful synthesis of IrO_2 nps was confirmed on all the three supports.

The structural confirmation and the uniformity of elemental distribution were confirmed by SEM-EDX analysis. **Figure S3** shows the SEM images of BN-rGO (**a, b**) rGO (**c, d**), and c-BN (**e, f**) supports. BN-rGO sheets were obtained as highly exfoliated graphene sheets similar to that of rGO, whereas c-BN (flake size < 1 µm) had powder-like appearance. Further, **Figure S4** show the EDX mapping analysis of IrO_2-BN-rGO which confirmed the hmogeneous distribution of the respective elements in the catalyst. The doping amount of B and N in BN-rGO was estimated to be 9.4 and 11.5 wt.% with Ir decoration of 12.1 wt.%. For IrO_2-rGO and IrO_2-c-BN (B: 27.2 wt.% and N:

Table 1 Particle size, np surface area, and mean lattice spacing values for the synthesized catalysts, estimated from TEM

Catalyst	Particle size (nm)	Np surface area[a] ($m^2 g_{Ir}^{-1}$)	Mean lattice spacing of support (nm)	Mean lattice spacing of IrO_2 np (nm)
IrO_2-rGO	1.5 ± 0.4	40.10	0.36 ± 0.02	0.23 ± 0.01
IrO_2-BN-rGO	1.7 ± 0.1	36.56	0.34 ± 0.01	0.23 ± 0.02
IrO_2-c-BN	1.6 ± 0.3	36.08	0.32 ± 0.03	0.23 ± 0.01
[a] calculated from TEM				

37.6 wt.%), the Ir amounts were estimated to be 11.7 and 11.2 wt.%, respectively. The Ir loading amount was further confirmed from MP-AES measurements for the three catalysts (**Table S2**). The estimated Ir amounts of 12.1, 11.2 and 11.7 wt.% in IrO_2-BN-rGO, IrO_2-c-BN, and IrO_2-rGO, respectively, were used for the estimation of mass activity in electrochemical measurements. We further calculated the np surface area of the catalysts using their average particle diameter and Ir wt.%. Normally, Brunauer-Emmett-Teller (BET)[45] method is used for evaluation of surface area. In our present work, we have calculated the np surface area from TEM since the supports used here are highly exfoliated supports that are known to exhibit high surface area. Both rGO and BN-rGO are prepared via the same method of pyrolysis at 1000 °C in N_2 atmosphere. The surface area calculated from BET analysis is the total surface area of the whole material including that of the exfoliated support, masking the surface area of the actual deposited nanoparticle catalyst, whose activity is being determined. Alternatively, electrochemically active surface area (ECSA) is determined from the hydrogen adsorption charge (H_{upd}) in the negative scan in CV in N_2 saturated electrolyte after double layer charging correction.[46] Often measured for Pt catalysts for ORR, the H_{upd} method has been validated versus CO adsorption and Cu under-potential deposition methods for Pt, Ir, Rh and Ni. In the case of IrO_2, the mechanism of underpotential deposition (H_{upd}) of H onto IrO_2 surface is not same as that of Pt which makes it difficult to determine the ECSA and has significant practical implications on benchmarking the anode catalyst performance.[47] Therefore, we preferred to estimate the np surface area from TEM particle size instead of using H_{upd} method or BET analysis. The np surface area of IrO_2-BN-rGO, IrO_2-c-BN and IrO_2-rGO was calculated (from TEM) to be 36.56, 36.08 and 40.10 $m^2 g_{Ir}^{-1}$, respectively (**Table 1**).

The reduction of GO to rGO and the introduction of defects due to BN-co-doping were confirmed by Raman spectroscopy. **Figure 3a** shows the Raman spectra of GO, rGO, BN-rGO, and c-BN. The Raman spectrum of GO consisted of two distinct peaks at 1350 cm^{-1} (D peak) and 1595 cm^{-1} (G peak) corresponding to the breathing mode of the sp^2 C ring and in-plane C=C sp^2 bond vibration, respectively.[48] The same peaks were observed in rGO at 1349 and 1590 cm^{-1}. A slight red shift of G peak in rGO is attributed to the lattice restoration of the graphene conjugate structure during high temperature pyrolysis.[49] Additionally, this shift also occurs when graphene is doped with heteroatoms, because G peak is dependent on charge carriers and dopant concentration.[50] Similar to GO and rGO, BN-rGO also showed two distinct peaks at 1343 and 1599 cm^{-1} due to the graphene framework. The intensity of G peak was observed to be lower and the peak was broader compared to rGO and GO. High intensity of the D peak arises as a result of creation of defects due to heteroatom doping (B and N). For c-BN, a single high intensity sharp peak was observed at 1366 cm^{-1}, referred to as G band in h-BN, corresponding to the E_{2g} vibration in h-BN.[51,52] The ratio of intensity of D and G peaks (I_D/I_G), which is commonly used to estimate the degree of induced defects and disorderness in the graphene structure, for GO, rGO and BN-rGO were ca. 0.89, 0.97 and 1.36, respectively. The significantly high I_D/I_G ratio for BN-rGO indicated towards the introduction of defects either due to heteroatom doping or the cracking of sp^2 carbon bonds at high synthesis temperature.[53] Additionally, during the high temperature annealing and reduction, the removal of carbon atom along with removal of oxygen functional groups of GO can also occur leading to creation of hole-like defects in graphene, contributing to an increase in D peak intensity.[54] However, on comparing the I_D/I_G ratio of rGO and BN-rGO, it can be deduced

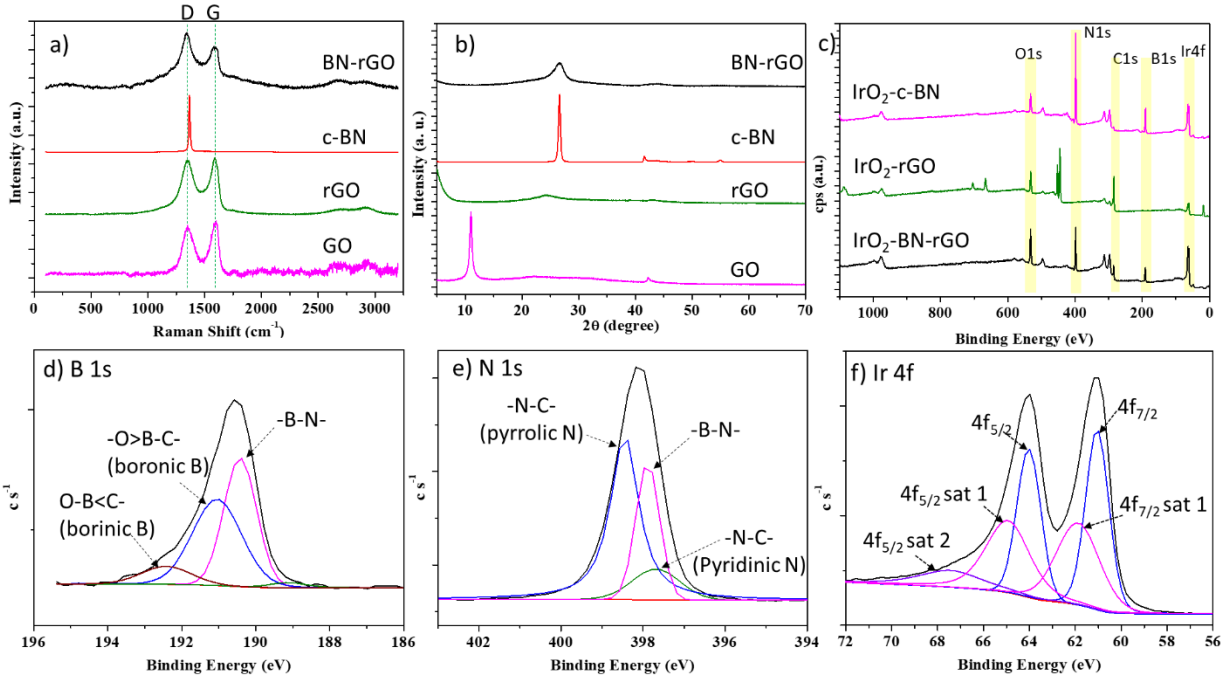

Figure 3 a) Raman spectra and **b)** XRD patterns of GO, rGO, c-BN and BN-rGO; **c)** Survey scan comparison of IrO_2-BN-rGO, IrO_2-rGO, and IrO_2-c-BN. Deconvoluted **d)** B 1s, **e)** N 1s, and **f)** Ir 4f spectra for IrO_2-BN-rGO.

that the high intensity of D peak in BN-rGO is majorly due to the doping of heteroatoms.

The crystalline structures of the synthesized samples were studied by XRD analysis. **Figure 3b** shows the comparison of the XRD profiles of GO, rGO, BN-rGO and c-BN. The *d*-spacing for GO was calculated to be 0.81 nm, arising due to the expansion of basal planes in the presence of oxygen functional groups. After reduction to rGO, the *d*-spacing reduced to 0.37 nm (2θ = 24.0°) due to the removal of oxygen functional groups. For BN-rGO, a broad peak at 2θ = 26.5° was observed implying the presence of B and N in graphitic-like structure of rGO. The *d*-spacing change in BN-rGO after reduction and heteroatom doping of GO, to 0.34 nm, is caused due to doping of the binary atoms (B and N) and additional removal of functional groups, indicating successful reduction of GO and simultaneous doping (**Table S3**). In addition, the peak sharpness indicated increased crystallinity of the sample. **Figure S5** shows the XRD profiles of the catalysts (IrO_2-rGO, IrO_2-BN-rGO and IrO_2-c-BN). After IrO_2 decoration, an additional broad peak at 2θ =40.3° was observed corresponding to (200) plane of IrO_2 [55] in all three catalysts.

The confirmation of BN-co-doping, type of B, N functionalities, and the amount of dopants were estimated by XPS analysis. As reported earlier, individual N and B can be doped in graphene lattice via formation of various functional groups, viz. pyridinic (N-6), pyrrolic (N-5), graphitic (N-G), and N-oxides (N-O) structures for N-doping[45] and boronic (BCO_2), borinic (BC_2O) and graphitic (B-G) structures for B-doping.[17] When B and N are present together, there is an additional possibility of formation of B-N bond. **Figure 3c** shows the XPS survey scan of IrO_2-BN-rGO with the presence of B, N, C, O and Ir elements at ~190, ~398, ~284, ~532 and ~64 eV respectively. A comparison with survey scan of IrO_2-rGO and IrO_2-c-BN is also provided. IrO_2-rGO showed only the presence of C, O and Ir in the catalyst. For all the catalysts, the corresponding B 1s, N 1s and Ir 4f peaks were deconvoluted centering the C 1s peak at 284.5 eV corresponding to sp^2 C=C bond. **Figure 3d-f** show the deconvoluted spectra for IrO_2-BN-rGO for B 1s, N 1s and Ir 4f peaks. Both B 1s and N 1s deconvolution reveal the presence of B-N bond centred at 190.4 (**B**-N) and 397.9 eV (B-**N**), respectively.[29] To confirm the presence of B-N bond, the spectra were compared with that of IrO_2-c-BN (**Figure S6d,e**). In B 1s and N 1s spectra of IrO_2-c-BN, B-N peaks centered at 190.3 and 397.8 eV, respectively, were observed which were similar to that in IrO_2-BN-rGO. Generally, it is possible to synthesize a disordered, amorphous B-N bond using BA and urea in nitrogen atmosphere at temperatures more than 1000 °C.[56] The involved reaction is following:

$$B_2O_3 + CO(NH_2)_2 \rightarrow 2\ BN + CO_2 + 2\ H_2O\ (T > 1000\ °C)$$

Therefore, on an rGO framework, doping with BA and urea via pyrolysis can result in occurrence of both types of reactions simultaneously, i.e. **a)** formation of a B-N pair at 1000 °C, and **b)** formation of other functionalities, such as B-C and N-C groups. This was confirmed by deconvoluted B 1s and N 1s spectra of IrO_2-BN-rGO. Along with B-N bond, the peaks derived from B-C (191.5 eV), B-O (192.9 eV) and B-H (organoborane derivatives, possibly at the edges, 189.6 eV)[17] functionalities were also observed in the B 1s spectrum of IrO_2-BN-rGO. Similarly, in the N 1s spectrum, functionalities referring to N-C bond, formed due to pyridinic (397.2 eV) and pyrrolic (398.6 eV)[45] groups were also observed. The formation of B-N pair occurs due to the higher bond energy of B-N bond (4.00 eV) compared to C-C (3.71 eV), B-C (2.59 eV) and N-C (2.83 eV) bond, indicating higher stability of B-N and C-C bonds.[57,58] Further, due to shorter bond length of B-N bond (1.45 Å) than B-C (1.49 Å) and comparable bond length to N-C (1.42 Å) and C-C (1.43 Å) bonds,[58] it is easier for the B-N pair to form in the presence of both BA and urea on an rGO framework. Theoretically, the comparable values of formation energies for B-doped graphene, N-doped graphene and bonded B-N co-doped graphene are reported to be −27.31, −30.94, and −29.24 eV, respectively, studied on a 2D graphene nanosheet in the xy-plane with a 2 × 2 × 1 super-cell using the Perdew-Burke Ernzerhof exchange and correlation (XC) functionals of the generalized gradient approximation.[59] These values depend on the input structure and the position of B, N and C atoms during theoretical simulations and hence, can change depending on the structure. Post-heteroatom doping, a charge redistribution is induced in the graphene lattice. The introduction of B and N functionalities breaks the lattice symmetry and open the band-gap in graphene due to the push and pull of nitrogen and boron atoms. A single pair of doped B-N is reported to introduce an ionic character in the bond with net charges of -1.54e on N and +1.82e on B.[58] Such a presence of alternative charges renders stability to the overall structure by increasing the binding energy, compared to B-B and N-N bonds,[27,58] and by reducing the net energy of formation of heteroatom-doped rGO framework.[27] This indicates that like c-BN, B-N bond in BN-rGO has the potential to provide chemical stability and resistance towards electrochemical corrosion to IrO_2 nps.[29]

For the three catalysts with IrO_2 nps, Ir 4f deconvolution was done to find the oxidation states of Ir deposited on the doped support and rGO. In literature, Ir^0, Ir^{IV} and Ir^V/Ir^{III} oxidation states of Ir ($4f_{7/2}$) for Ir-based catalysts are reported at 60.8, 61.7 (with a satellite peak at 1 eV higher binding energy), and 62.3 eV (usually observed after or during OER analysis due to the formation of O^{I-} species), respectively.[60] For all the oxidation states of Ir, the spin-orbit doublets of $4f_{7/2}$ and $4f_{5/2}$ appear as two distinct coupled peaks along with their corresponding satellite peaks, with a separation of ~3.00 eV. The $4f_{7/2}$ and $4f_{5/2}$ peaks at 61.1 and 64.1 eV, respectively, on IrO_2-BN-rGO catalysts corresponded to Ir^{IV} oxidation state, and their corresponding satellite peaks were also observed at 62.5 eV for $4f_{7/2}$ and, 65.3 and 67.0 eV for $4f_{5/2}$ states. These peaks were in correlation with the XRD peak at 40.3°, which relates to the (200) plane of IrO_2 rutile crystal (**Figure S5**), as reported in literature.[61] However, the Ir 4f peaks in IrO_2-BN-rGO (**Figure 3f**) were shifted 0.7 eV lower than rutile type unsupported IrO_2 (peak positions at 61.8 and 64.8 eV) and 0.3 eV lower IrO_2 on non-doped support (IrO_2-rGO) (**Figure S6b**). The peaks were at a difference of 0.2 eV binding energy than Ir powder (metallic Ir^0 peaks at 60.9 and 63.9 eV) (**Figure S6a**). Commonly, the shift

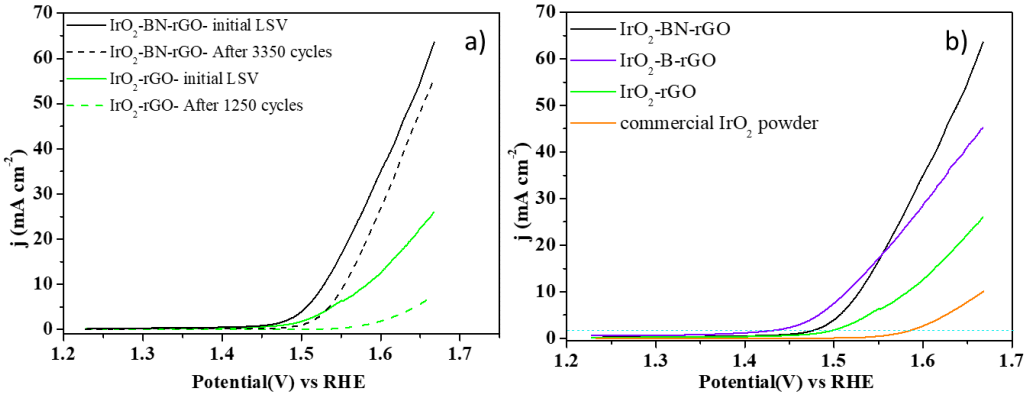

Figure 4 LSV profiles of **a**) IrO_2-BN-rGO and IrO_2-rGO catalysts before (solid line) and after (dashed line) 3350 and 1250 cycles of ADT, respectively between 1.20 to 1.65 V vs RHE in 0.5 M H_2SO_4 solution. **b)** Current density change of LSV on IrO_2-BN-rGO (12.1 wt.% Ir, particle size: 1.7 nm), IrO_2-B-rGO (19.6 wt.% Ir, particle size: 1.5 nm[17]), IrO_2-rGO (11.7 wt.% Ir, particle size: 1.5 nm), commercial IrO_2 powder (particle size: 60-90 nm) measured in 0.5 M H_2SO_4 solution between 1.20 to 1.65 V vs RHE.

in the peak positions or the change in binding energy of Ir 4f peaks indicates the modulated electronic states or charge transfer between metal nps and support because of the existing electrostatic interactions. **a)** The transfer of electrons from N functional groups to IrO_2 nps and **b)** simultaneously from IrO_2 nps to C bonded to B-N pairs, and B-C functionalities is expected to bring a shift of Ir 4f binding energy to a lower value compared to rutile type unsupported Ir^{IV} peaks, leading to a strong metal-support interaction (SMSI) between IrO_2 nps and BN-rGO support. The peak positions of Ir 4f and their shifts for the studied catalysts are tabulated in **Table S4**. The peak shift arising due to interaction of IrO_2 nps with support confirmed the successful formation of IrO_2-BN-rGO.

Electrochemical characterization. The OER electrocatalytic activity of the synthesized catalyst, IrO_2-BN-rGO, was estimated using LSV in 0.5 M H_2SO_4. **Figure 4a** shows the LSV profiles of IrO_2-BN-rGO and its comparison with that of IrO_2-rGO. The onset potential (the point in non-faradaic region where slope starts increasing) for IrO_2-BN-rGO was observed to be 1.48 V, which is 0.04 V higher than our previously reported work using B-rGO as a support,[17] owing to the presence of B-N bonded pair (non-conductive), but 0.13 V lower than commercial IrO_2 powder (**Figure 4b, Table S5**). Further, the current density obtained at 1.65 V was estimated to be 55 mA cm^{-2}. This value is *twice* of that observed on IrO_2 nps on B-rGO support[17] (single atom-doped), ~2.5 times higher than that on IrO_2 nps on the undoped support (**Figure 4**) and ~4 times of that on IrO_2 nps on c-BN support (**Figure 4b**). Additionally, it is also ~10 times higher than that on the commercial IrO_2 powder (Ir loading amount: 287 µg cm^{-2}, **Figure 4b**). The np surface area normalized current density profiles of the three catalysts are shown in **Figure S7**.

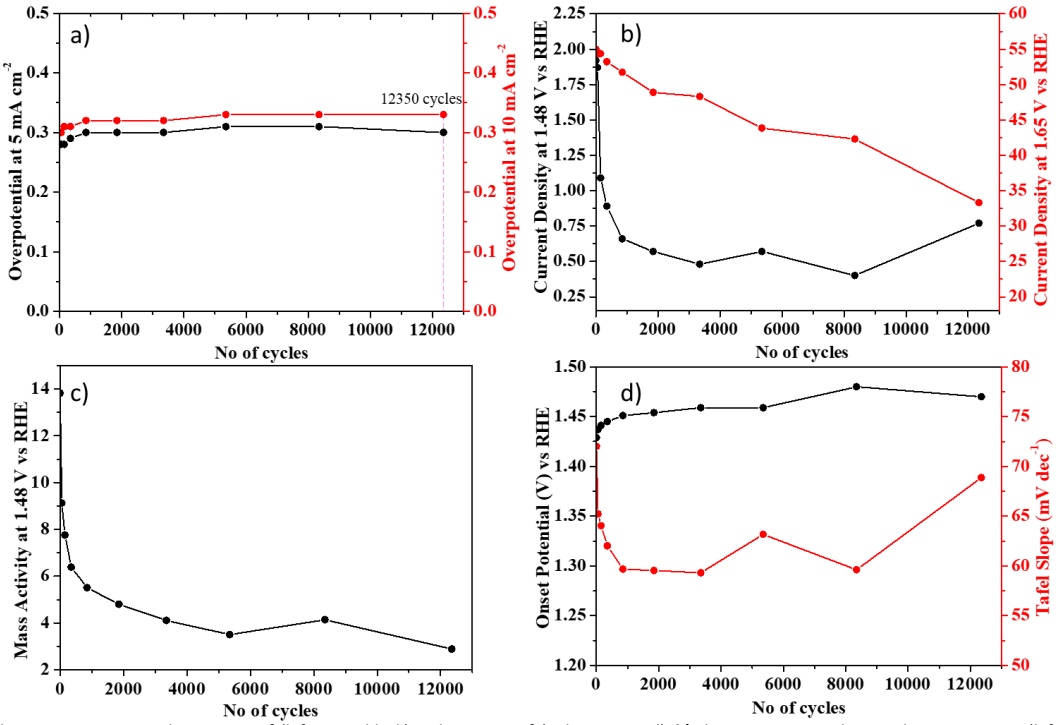

Figure 5 a) The change in overpotential at 5 mA cm^{-2} (left y-axis-black) and 10 mA cm^{-2} (right y-axis-red), **b)** change in current density change at 1.48 V (left y-axis-black) and 1.65 V (right y-axis-red), **c)** change in mass activity at 1.48 V, and **d)** change in onset potential (V) (left y-axis-black) and calculated Tafel slope (mV dec^{-1}) (right y-axis-red) with increasing number of cycles on IrO_2-BN-rGO.

The significantly high difference in the current density among synthesized catalysts (IrO_2-rGO, IrO_2-BN-rGO and IrO_2-c-BN) and commercial IrO_2 powder is because of small specific surface area of commercial IrO_2 powder (particle size: 60-90 nm) compared to synthesized IrO_2 nps in the present study. For IrO_2-BN-rGO, the participation of an electronically conductive support along of small size IrO_2 nps (1.7 nm) results in significantly high current densities. In case of IrO_2-rGO, the catalyst showed poor activity compared to its doped counterpart despite the smaller size of IrO_2 nps (high np surface area). IrO_2-BN-rGO owes its enhanced catalytic activity to the heteroatom dopants. The presence of heteroatoms in the lattice can result in two distinct phenomena, **1)** the opening of band gap of graphene lattice and **2)** strong metal-substrate interaction (SMSI) between IrO_2 and BN-rGO support. A conductive support can interact beneficially with the deposited metal centres greatly influencing their morphology, reactivity, and stability owing to stronger interactions between metal and support. The catalyst on BN-rGO support showed better electrochemical performance than IrO_2 nps on rGO, single atom doped rGO (B-rGO[17] and N-rGO[18]), commercial IrO_2 powder and other reported precious metal catalysts (**Table S5**). These results depict that biatomic doping in the catalyst support enhances the electrocatalytic performance of the deposited metal oxide catalysts.

Accelerated durability Tests (ADT). To estimate the durability of the designed catalysts, ADT was performed on the catalysts by cycling the catalyst for *n* number of cycles (*n* = 50, 100, 200, 500, 1000, 1500, 2000, 2500, 5000) between 1.0 to 1.3 V vs RHE at 50 mV s^{-1}. The number of cycles was increased gradually and LSV was measured at each step to monitor the changes in the electrochemical parameters such as current density, overpotential, onset potential, mass activity and Tafel slope. The ADT analysis was stopped when the catalyst started peeling from the GC electrode. The remaining catalyst on GC was dispersed in IPA and drop-casted on a Cu grid and Si substrate for post-mortem analysis via TEM and XPS, respectively. The following sections discuss the observed changes during durability tests for IrO_2-BN-rGO and compare them with IrO_2-rGO. The additional comparison with IrO_2-c-BN is provided in the ESI (**Figure S10 and Table S8**).

a) Effect of ADT on Overpotential

A slight increase in overpotential was observed both at 5 and 10 mA cm^{-2} after 3350 and 12350 cycles (**Figure 5a**) for IrO_2-BN-rGO. The initial sudden increase in overpotential with number of cycles is caused by the decreased loading of catalyst, occurred due to the detachment of the IrO_2 nps responsible for initiating the reaction. Along with the remaining nps, the next step involves the contribution of the support (acting as co-catalyst, providing np surface area) to advance the reaction and to prevent further loss of the nps.[62] In the case of BN-rGO, the conductive carbon framework with high intrinsic current density is expected to interact electrostatically with IrO_2 nps, and hence, mitigate the loss of nps during the course of reaction. Due to this, the increase in overpotential for OER on IrO_2-BN-rGO was suppressed over 12350 cycles (0.30 to 0.33 V, i.e. only ~20 mV of overpotential degradation was observed after 3350 cycles, and 10 mV from 3350 to 12350 cycles). For IrO_2-rGO, the overpotential increased from 0.35 V to 0.46 V over 1250 cycles due to **a)** the initial detachment of some IrO_2 nps and **b)** the lack of contribution of rGO support in the catalytic reaction due to the low intrinsic current density of rGO compared to BN-rGO. These factors lead to an overall overpotential degradation of 108 mV over 1250 cycles for IrO_2-rGO.

b) Effect of ADT on Current Density and Mass Activity

A similar effect of ADT was also reflected in current density profile (**Figure 5b**). As expected, for all the catalysts, the current density decreased with increasing number of cycles, due to the adsorption of intermediates formed during OER.[63] However, in the case of IrO_2-rGO, the current density of the catalyst decreased to 75 % of the original value after 1250 cycles while the peeling of the catalyst from GC initiated in 850 cycles. The current density at 1.65 V on IrO_2-BN-rGO dropped 12 % of the initial value after 3350 cycles and 39 % after 12350 cycles when the catalyst came-off of GC electrode. This points towards the significance of doped rGO framework as support that helps in providing significant current densities even after ~45 h (12350 cycles). As the reaction proceeded, the adsorption of intermediates at the electrode surface and continuous np degradation resulted in decrease of the net np surface area responsible for catalysis, leading to further decreased current densities. The change in mass activity (**Figure 5c**), estimated from current density corresponded with the above explanation. With the propagation of OER, slow detachment and degradation of IrO_2 nps occurs and hence, the overall loading amount of active catalyst decreases, thereby decreasing the mass activity. The description is schematically represented in **Figure 6**, along with interpretation of Tafel slope.

c) Effect of ADT on Tafel Slope

A plot of Tafel slope vs no. of cycles, for IrO_2-BN-rGO, is shown in **Figure 5d**, along with the change in the onset potential with increasing number of cycles. The Tafel slope quantitatively formulates the relation between applied potential and observed current,[64] and qualitatively analyses the corresponding reaction kinetics of the electrode. For practical reactions with multiple steps like OER, great uncertainties arise while interpreting the reaction mechanism because of the complex set of reactions subjective to the electrode nature and electrolyte medium. OER also involves multiple reaction routes with the formation of many possible intermediates such as OH, O and OOH.[64] It is usually understood that the first step of OER is given by a one-electron transfer reaction corresponding to a Tafel slope of 120 mV dec^{-1} if this step is the rate-determining step (rds). However, this value changes depending on the subsequent steps for different catalytic materials or if the reaction steps are either electron transfer steps or chemical steps such as association or dissociation. When a chemical reaction step after an electron transfer step is an rds, the Tafel slope value becomes 60 mV dec^{-1}. For multistep reactions such

as OER (a 4-electron transfer system), systems like Ni-Bi have shown Tafel slopes of 30 mV dec^{-1} with the third electron transfer step as rds.[64] For IrO_2, Tafel slopes of 40 and 60 mV dec^{-1} are reported in acidic solutions ($HClO_4$ and H_2SO_4 solution) on GC and Ir substrates.[64] Additionally, for carbon based OER catalysts, estimated Tafel slopes in alkaline solutions (0.1/1 M KOH) are 72, 140, 120, 68.5 and 83 mV dec^{-1} for electrochemically activated multi-walled carbon nanotubes (CNTs),[65] nitrogen doped graphene–CNT,[66] graphitic carbon nitride (g-C_3N_4),[67] graphene- g-C_3N_4,[67] and CNT-3D g-C_3N_4,[68] respectively. Therefore, it is not justified to interpret the mechanism of OER just based on Tafel slope. Nonetheless, we can still get some useful information regarding the kinetics and intermediate adsorption for our novel catalyst, IrO_2-BN-rGO.

For IrO_2-BN-rGO, the Tafel slope was estimated to be 72.1 mV dec^{-1} for the initial LSV, which decreased to 59.3 mV dec^{-1} over 3350 cycles (**Figure S8b, Table S6**). This value of Tafel slope for IrO_2-BN-rGO is lower than that on Ir surface in 1.0 M H_2SO_4 at 80 ^oC,[69] indicating faster reaction kinetics than Ir). For IrO_2-rGO, a significantly high Tafel slope of 98.0 mV dec^{-1} was obtained for the first LSV which decreased to a value of 56.9 mV dec^{-1} over 1250 cycles (**Figure S9b, Table S7**). The different initial values of Tafel slope for IrO_2-BN-rGO and IrO_2-rGO can either be an indication of dissimilar reaction mechanisms or related to the different strength of adsorption of intermediates at the electrode surface due to the different conductive nature of the supports. For IrO_2-BN-rGO, due to the deposition of IrO_2 on BN-rGO surface, the Tafel slope for the initial LSV was obtained similar to that of carbon-based composites as mentioned above. With increasing number of cycles, the Tafel slope slightly decreased to 59 mV dec^{-1} **(Figure 6a)** indicating the eased reaction and stronger adsorption of intermediates at the electrode surface in the initial stage of reaction (**Stage I**). Commonly, increase in the adsorption energy of intermediates is also associated to decrease in active surface area, leading to slower rate of reaction, marked by an increase in the Tafel slope.[64] However, for IrO_2-BN-rGO, the Tafel slope decreased till 3350 cycles pointing towards the faster conversion of the adsorbed intermediates to O_2 and further, unhindered O_2 evolution. The value remained near 60 mV dec^{-1} up to 8350 cycles, (**Stage II**), confirming no change in reaction mechanism and efficient conversion of oxygen intermediates to O_2. However, the np surface area was slightly affected (slight deviation in the Tafel slope). Further, after 8350 cycles, the Tafel slope gradually increased to ca. 68.8 mV dec^{-1} due to a reduction in the available surface area caused by exhaustive adsorption of intermediate species and degradation of the nps and support (**Stage III**). The changes in Tafel slope are supported by change in other electrochemical parameters, viz. increased

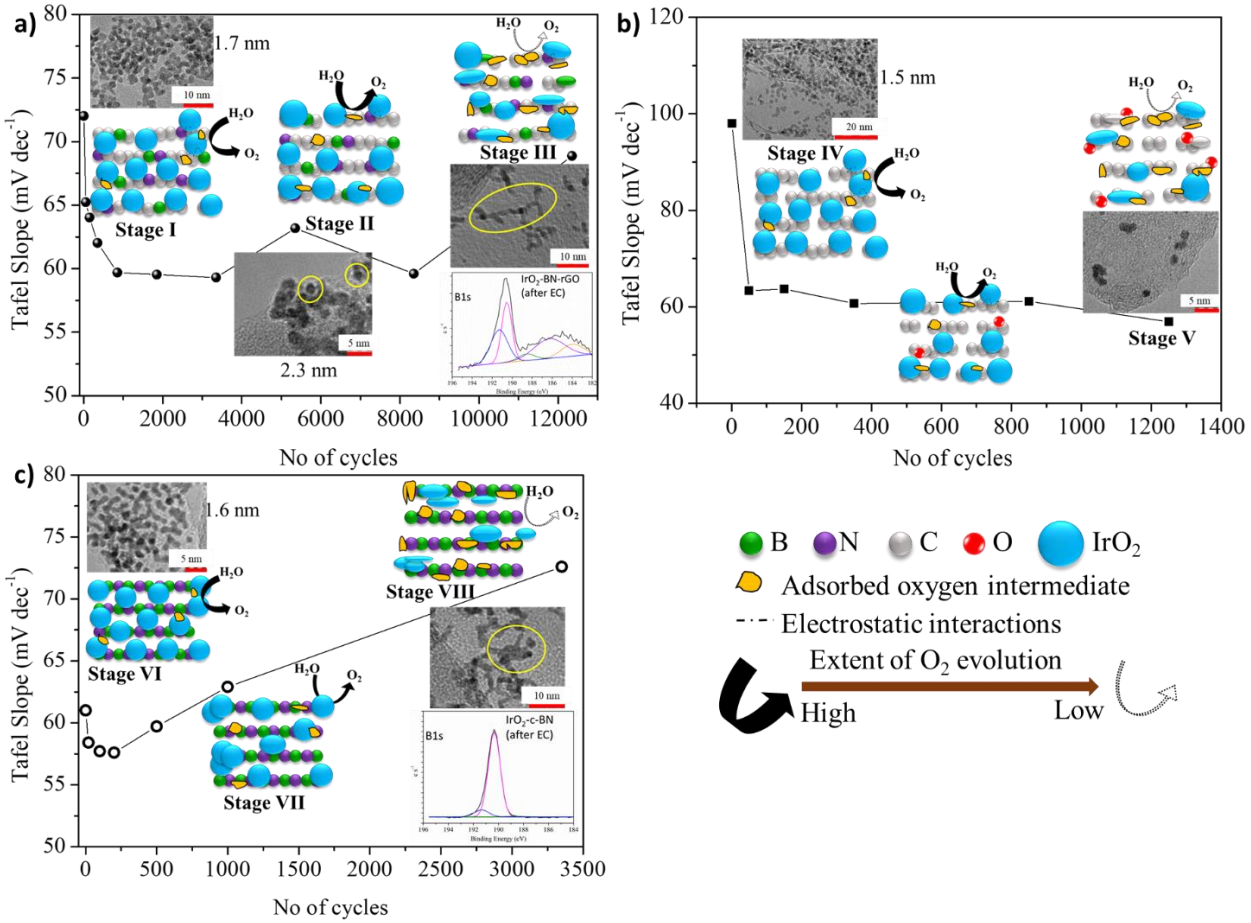

Figure 6 Schematic representation of catalyst degradation observed by the change in Tafel slope with respect to the number of cycles for **a)** IrO_2-BN-rGO, **b)** IrO_2-rGO and **c)** IrO_2-c-BN. The changes in the morphology and chemical structure observed at the corresponding stage in TEM and XPS, respectively, are also provided. The colour representations are given in the inset.

overpotential (by 30 mV), and reduced current density (by 39%) after 12350 cycles. For IrO_2-rGO (**Figure 6b, Stage IV and V**), the Tafel slope for the first LSV was observed to be 98.0 mV dec^{-1} which decreased to 63.3 mV dec^{-1} in 50 cycles and showed slight variation till 1250 cycles. The value of Tafel slope for higher no. of cycles in IrO_2-rGO was similar to that of IrO_2-BN-rGO and other reported IrO_2 catalysts.[64] Although the Tafel slope was retained at an optimum value for IrO_2-rGO, the drastic decrease in current density indicated towards the continued adsorption of the reaction intermediates with slow O_2 evolution on the surface of IrO_2-rGO leading to reduced densities. In case of c-BN support (**Figure 6c**), the Tafel slope was observed similar to that of IrO_2[64] (61.0 mV dec^{-1}) due to the negligible contribution of c-BN towards improvement of OER activity. OER catalysed by IrO_2 nps at the initial stage of reaction resulted in a significant amount of current density and hence, a slight decrease in the Tafel slope was observed (**Stage VI**). With increasing number of cycles, loss/disintegration of IrO_2 nps and adsorption of intermediate species at the catalyst surface occurred (**Stage VII**). Poor conduction of c-BN support led to inefficient conversion of oxygen intermediates to O_2 and disintegration of IrO_2 nps, leading to a large increase in Tafel slope (~72 mV dec^{-1}, **Stage VIII**), as reported for IrO_2 on TiO_2.[70]. **Figure S8** and **Table S6** summarize the change in all the electrocatalytic parameters calculated from the LSV profile viz. η (mV) at a current density (j) = 5 and 10 mA cm^{-2}, j (mA cm^{-2}) at η = 250 and 450 mV, onset potential (V), Tafel slope, b (mV dec^{-1}), and mass activity at η = 250 mV (1.48 V) for IrO_2-BN-rGO. Similar parameters calculated for IrO_2-rGO and IrO_2-c-BN are shown in **Figure S9/Table S7 and Figure S10/ Table S8, respectively.**

Discussion. The difference in the OER behaviour of the catalysts mainly arises from the dissimilar interaction between the supports and IrO_2 nps. It is hard to comment on the magnitude of participation of individual functionalities in BN-rGO support in the reaction. Altogether, the enhanced catalytic activity and remarkable durability of IrO_2-BN-rGO catalyst can be due to several factors, namely, **a)** defects generation in graphene due to heteroatom doping, **b)** increased surface area due to rGO matrix, **c)** creation of localized active centres due to the presence of B-N, B-C and N-C functional groups, and **d)** increased hydrophobicity[71] and **e)** corrosion resistance due to B-N bond. Without heteroatom doping, the non-doped supported electrocatalyst (IrO_2-rGO) does not show any significant improvement in the electrocatalytic activity or durability. Further, when compared with single atom doped rGO,[17,18] the electrochemical properties of biatomic doped rGO are highly upgraded. At the atomic level, these properties can be confirmed with the help of other analytical techniques and atomic level theoretical simulations such as density functional theory (DFT)[72], synchrotron-based X-ray techniques, and near-edge X-ray absorption fine structure (NEXAFS)[27]. Due to the unavailability of these techniques at the current stage, we tried our best to infer our results from the combination of morphological and electrochemical analysis.

Post-mortem Analysis. The above inferences related to the change in structure of IrO_2 nps after 3350 and 12350 cycles are confirmed by TEM and XPS analysis after durability tests (also shown in insets of **Figure 6**). **Figure 7 (a-d)** shows the change in morphology of IrO_2 nps after ADT on BN-rGO support studied via TEM after 3350 **(Figure 7a, b)** and 12350 **(Figure 7c, d)** cycles of CV, respectively. The images show that the overall np surface area of the IrO_2 nps responsible for catalysis gradually decreased due to increment in particle size and aggregation of nps after 3350 cycles of CV. The diameter of the nps slightly increased to 2.3 nm and yet no significant change in the spherical shape was observed. However, after 12350 cycles, a deformed structure of IrO_2 nps was observed, due to the many reasons responsible for np degradation via routes such as agglomeration, Ostwald ripening, electrolytic dissolution of metal nps, and corrosion of the support material.[73] The complete shape disintegration of IrO_2 was further, confirmed by the change in lattice spacing (0.17 ± 0.02 nm) of IrO_2 nps after ADT (**Figure 8i**). Similar case was observed in IrO_2-rGO (after 1250 cycles) (**Figure S11 a, b, c**) and IrO_2-c-BN (after 3350 cycles) (**Figure S11 d, e, f)**. For IrO_2-rGO, the catalyst completely peeled-off of the GC electrode in 1250 cycles and current density reduced to insignificant value. As seen in **Figure S11c**, for IrO_2-rGO, the nps have undergone shape distortion along with aggregation, reducing the np surface area available for catalysis, resulting in the poor durability of the catalysts. The enhanced durability and stability of the IrO_2-BN-rGO catalysts is attributed dominantly to the synergy between IrO_2 nps and BN-rGO support. The degradation of nps in IrO_2-c-BN catalyst is more evident after 3350 cycles than the nano-carbon supported catalysts. This specifies that a 2D nano-carbon framework is crucial for improved interaction and structural stability of supported metal-oxide nps.

Post-mortem XPS of IrO_2-BN-rGO, IrO_2-rGO, IrO_2-c-BN and BN-rGO support was carried out after electrochemical evaluation after 12350, 1250, 3350 and 1550 cycles of ADT, respectively, after the catalyst started peeling from the GC electrode. A change in the atomic concentration of all the elements was observed between IrO_2-BN-rGO catalysts before and after ADT (**Figure 8a**). The intensity of the peaks for Ir (~61-64 eV), N (~398 eV) and B (~188 eV) elements reduced drastically and the peak intensity for O (~532 eV) increased (**Table S9**). Commonly, during OER, two major phenomena occur, **i)** adsorption of oxygen intermediates on the surface of the catalyst and **ii)** the carbon oxidation reaction (COR). The oxidation potential of carbon to CO_2 ($C + 2H_2O \rightarrow CO_2 + 4H^+ + 4e^-$) is 0.207 V RHE.[74] In the absence of water, the electrochemical carbon corrosion can be prevented even under harsh oxidative conditions. Jang *et al.* have reported that the presence of IrO_2 promotes water oxidation around the carbon supports which suppresses the oxidation of carbon to sustain the current flow through the cell.[75] Since, OER is electrochemically more feasible than COR[16], catalysts with high activity are known to mitigate COR. Yet, it is possible for OER to proceed in combination with COR which causes the loss of active carbon mass leading to the loss of supported metal-oxide

catalyst in highly oxidative conditions. XPS survey scan (**Figure 8a**) showed a substantial increase in the O 1s peak intensity, which can be dominantly due to the result of adsorption of oxygen intermediates during OER and to some extent, due to COR. This is also supported by the comparison of C 1s deconvolution of IrO_2-BN-rGO and IrO_2-rGO catalysts before and after ADT **(Figure S12 g, h**). For IrO_2-rGO, the oxidation of the support was prominent as observed from the shoulder peak in the C 1s deconvoluted spectrum after ADT referring to -C-O. For IrO_2-BN-rGO, the C 1s peak appeared broader due to the high intensity obtained after ADT, however, peaks referring to formation of C-O or C=O were not observed (**Figure 8c and S12g**). It is expected that the electrochemically stable B-N bond imparted stability to the BN-rGO support leading to its enhanced durability up to 12350 cycles.

As for other elements in IrO_2-BN-rGO, other than the change in intensity, no significant change in the peak profile of N 1s was observed (**Figure 8d, e**). Interestingly, a significant change was observed in the B 1s peak after ADT for IrO_2-BN-rGO as well as for BN-rGO support**,** respectively. A broad hump, corresponding to the formation of B-H adducts,[76] emerged at ~186 eV changing the peak positions and profiles for B 1s peak before and after ADT (**Figure 8b**). The hump was also observed slightly in BN-rGO support after 1550 cycles (**Figure S12e**). Deconvolution of the B 1s peak after ADT (**Figure 8g**) showed that the peak positions of B-N within the lattice and B-O bonds at the edges were retained at higher binding energies whereas, the B-C bonded functional groups (C-B<O, C>B-O) were removed. The identity of other peaks at lower binding energies could not be referenced in the literature. However, we expect the presence of metal-bonded boron adducts at lower binding energies. It is reported that B 1s peak for metal bonded boron, metal-B-solvent adduct, and boron carbides (B_4C) type of B-based materials appear in the range of 186-188 Ev.[76] We ruled out the possibility of B_4C formation as it requires temperatures higher than 1000 ^oC, or the presence of a catalyst.[78,79] Further, any potential dependent synthesis of B_4C is also not known. Therefore, the formation of B-H entities or metal bonded B-H adducts at lower binding energies is acceptable.[76] We compared our XPS results for B 1s peak of IrO_2-BN-rGO with that of IrO_2-c-BN. The broad hump at ~186 eV, referring to metal-bonded boron adducts was only observed in the case of IrO_2-BN-rGO and not in IrO_2-c-BN (**Figure 12c**), owing to the presence of weaker B-C functional groups in IrO_2-BN-rGO than the entire collection of B-N bonds in IrO_2-c-BN. This further indicated towards the higher electrochemical stability imparted by the B-N bond in IrO_2-BN-rGO.

Along with B 1s peaks, a profile change of Ir 4f peaks was also observed for IrO_2-BN-rGO after ADT (**Figure 8f**). The Ir 4f peak for IrO_2-BN-rGO showed a low intensity broad line shape which was deconvoluted into the corresponding doublets as explained earlier. After ADT, the Ir 4f doublets (**Figure 8h**) were shifted 0.3 eV to *higher* binder energy, indicating the loosening of interaction between the support and IrO_2 nps. The presence of metallic Ir peak in deconvoluted Ir 4f spectrum of IrO_2-BN-rGO indicated the formation of metallic Ir adducts due to the collapse of IrO_2 structure during the OER[60]. For IrO_2-rGO, the Ir 4f peaks after ADT were completely distorted (**Figure S12b**)

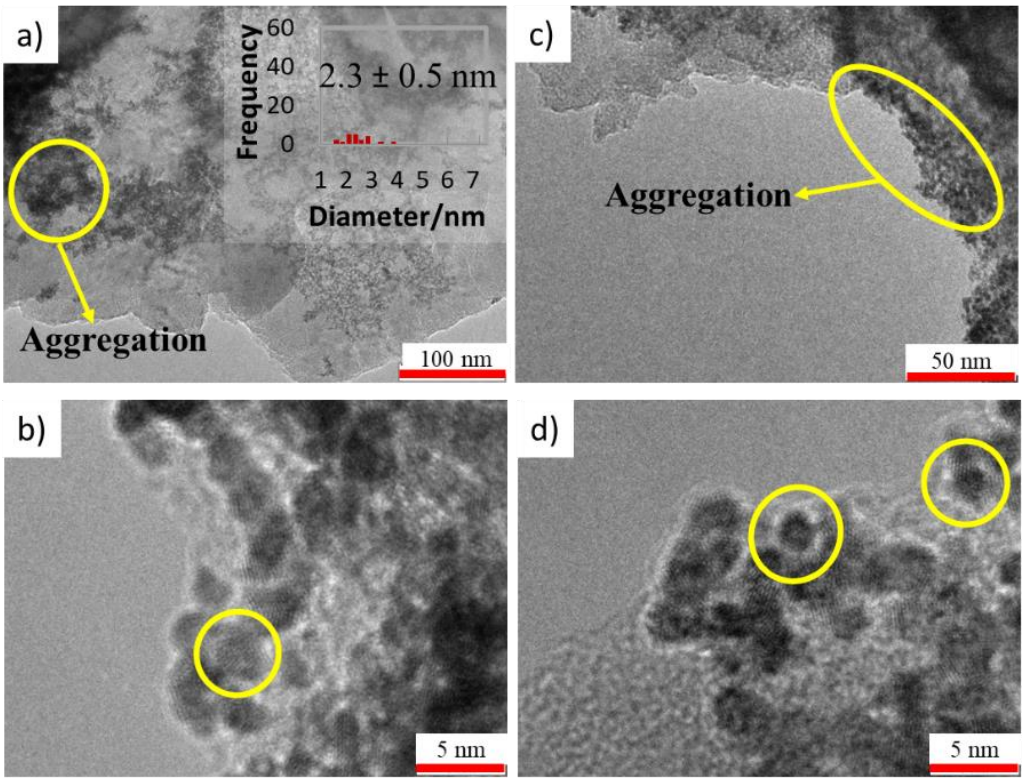

Figure 7 TEM images of IrO_2- BN-rGO after (**a, b**) 3350 cycles (**a.** inset: particle size and size distribution of nps after EC), (**c, d**) 12350 cycles of ADT indicating initiation of degradation of IrO_2 nps via shape distortion and aggregation of particles.

indicating the complete disintegration of the Ir structure during ADT (1250 cycles) due to the poor interaction with the support and reduced stability. The peaks did not refer to any Ir configuration present in literature. The deconvoluted Ir 4f spectrum of IrO_2-c-BN is also provided in **Figure S12f**.

Post-mortem XPS spectrum and TEM images for the studied catalysts signify the fact that a conductive rGO framework plays a vital role in improving the activity and stability of the metal-oxide catalyst. With the collapse of the metal-oxide structure, other metal-intermediate moieties can be formed during the electrochemical reaction on the surface of a conducting support, such as doped rGO. Our post-mortem results clarify that the catalyst degradation after 12350 cycles in IrO_2-BN-rGO occurs due to the loss of np surface area, collapse of original nanoparticle structure, and degradation of BN-rGO support caused by adsorbed oxygen intermediates and water molecules. However, they also validate the necessity of a conductive carbon framework to improve the durability of the catalyst and that conductive carbon supports can decelerate the rate and extent of Ir oxidation to a high extent. Our results evince that a conducting support like BN-rGO can permit **a)** stronger binding of IrO_2 nps, **b)** preventing their aggregation and degradation, and lead to **3)** higher electrochemical stability of such metal-support type composite OER catalysts. This study further demonstrates the advantage of having graphene with B-N pair in improving the electrochemical corrosion resistance of the composite-catalyst towards OER.

We have studied the synthesis and electrochemical performance of a novel and active catalyst for OER by implementing the concept of composite materials as electrocatalysts in the current work. Binary heteroatom doping of rGO with B and N proved to be effective to fabricate IrO_2 nps with advanced stability for OER in acidic medium. The presence of binary heteroatoms (specifically B and N) in graphene lattice can lead to several advantageous features, namely, **1**) the interaction between the metal particles and substrate (SMSI) is strengthened, **2**) the surface of BN-rGO becomes more hydrophobic,[71] due to the presence of B-N bonds, preventing the corrosion of carbon because of water molecules to an extent, and **3**) introduced B and N atoms can create more defects in graphene which not only act as active sites for catalyst attachment but also restrain the aggregation of

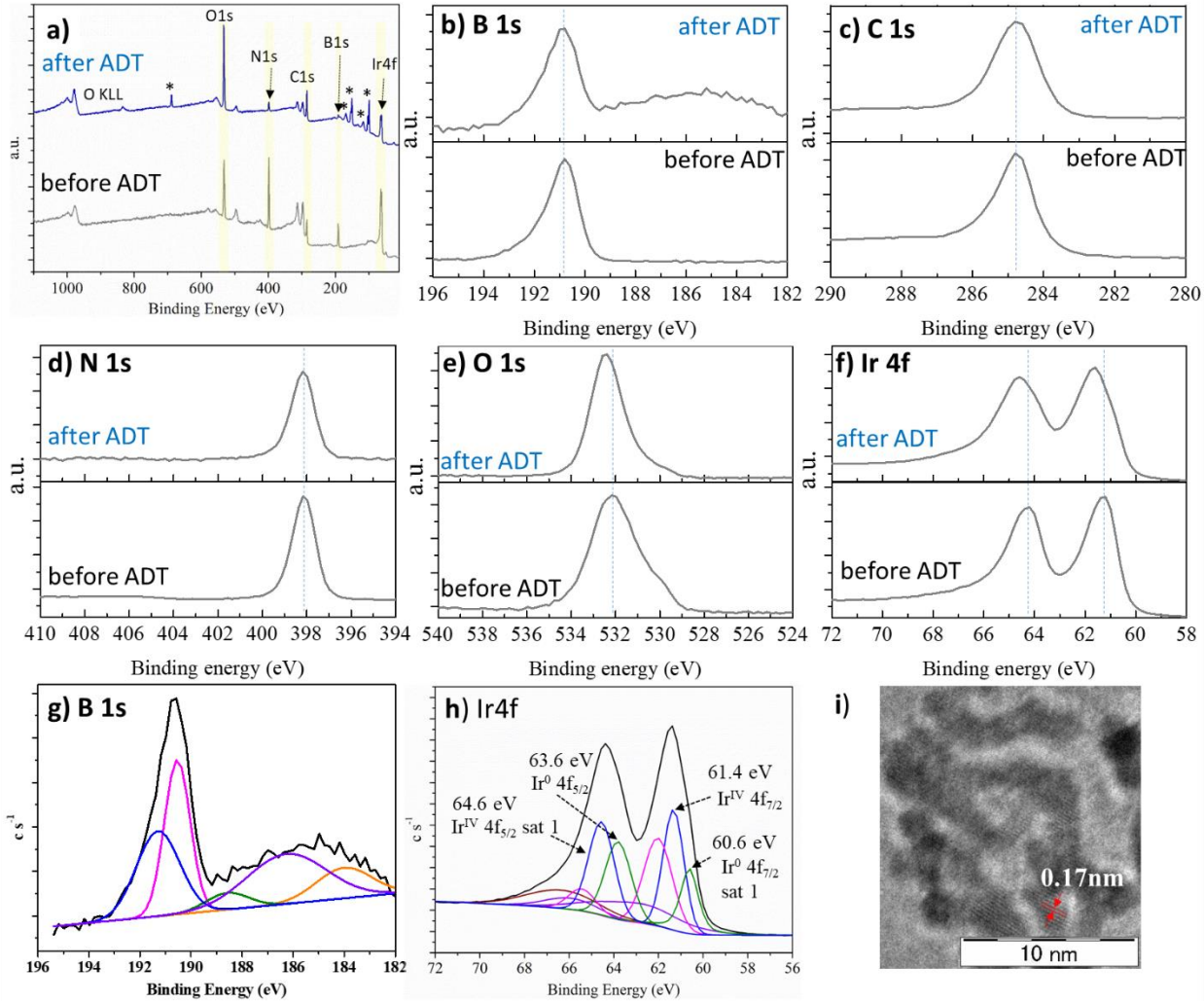

Figure 8 a) XPS Survey scan of IrO_2-BN-rGO before and after ADT (* peaks refer to Si 2p from Si substrate used for XPS analysis); comparison of **b)** B 1s, **c)** C 1s, **d)** N 1s, **e)** O 1s and **f)** Ir 4f spectra of IrO_2- BN-rGO before and after ADT; **g)** B 1s and **h)** Ir 4f narrow scan of IrO_2- BN-rGO after 12350 cycles of ADT and i**)** change in lattice spacing of IrO_2 np observed in the TEM image of IrO_2- BN-rGO after 12350 cycles of ADT.

deposited IrO_2 nps. All these advantages play their role in enhancing the catalytic activity of the IrO_2-BN-rGO catalyst. This concept opens up the possibilities of designing heteroatom doped graphene based hierarchical electrocatalysts for acidic medium electrolysis. However, further optimization of heteroatom doping and synthesis temperature is required to establish the acidic media OER catalysts and answer a few important questions like **a)** behavior of B-N species and **b)** charge transfer between the B-N functionalities and carbon support during the OER process. Extensively researched and ongoing *in-operando* techniques such as *in-operando* XPS, X-ray Absorption Spectroscopy (XAS) and *in-operando* Atomic Force Microscopy (AFM) can provide a solution to the issues related to the catalyst structure and reaction mechanisms which can open up possibilities of developing better catalysts.

Conclusions

In conclusion, we report the contribution of BN-co-doped rGO as a novel support for IrO_2 nps for OER. The designed catalyst, IrO_2-BN-rGO, showed high activity with low overpotential. The catalyst showed high durability for up to 3350 cycles with a low loading of Ir (140 μg cm^{-2}). To confirm B-N bond formation, we compared the chemical composition of our catalyst with IrO_2 nps supported on c-BN. Similar to c-BN, the presence of B-N bond was observed in the BN-rGO. Despite the presence of B-N bond in BN-rGO, high activity and significantly high durability were obtained due to the charge redistribution caused by different functional groups in the lattice. We compared our electrochemical results with that of IrO_2 nps deposited on non-doped support, rGO (IrO_2-rGO) which exhibited poor performance with a change in shape of the metal particles after 1250 cycles. For IrO_2-BN-rGO, the durability tests were further extended to 12350 (~45 h) cycles, until the catalyst peeled-off from the GC electrode. A low overpotential degradation of 30 mV was observed over a period of ~45 h. This is one of the most important pieces of evidence to prove the significance of the presence of conductive rGO or carbon framework in improving the electrochemical performance for acidic medium electrocatalysis. The origin of this synergistic effect arising due to the presence of structurally different untraceable defects, B-N and N-C/B-C, makes it very difficult to detail the mechanistic effect on OER. However, the design of such catalysts and study of similar conductive supports opens up possibilities of in-depth research towards electrocatalytic OER in acidic medium and will direct us towards designing unconventional catalysts for OER.

Author Contributions

PJ carried out the major research work and drafted the manuscript. RY helped in the durability tests. TI and YM guided in the MP-AES analysis. MH and MY supervised and guided during the research work

Conflicts of interest

There are no conflicts to declare.

Acknowledgements

This work was supported by Smart Energy Research Centre at Toyota Technological Institute, Nagoya, Japan and partially supported by Yashima Environment Technology Foundation.

References

1 Q. Shi, C. Zhu, D. Du and Y. Lin, *Chem. Soc. Rev.*, 2019, **48**, 3181–3192.
2 N. Danilovic, R. Subbaraman, K. C. Chang, S. H. Chang, Y. J. Kang, J. Snyder, A. P. Paulikas, D. Strmcnik, Y. T. Kim, D. Myers, V. R. Stamenkovic and N. M. Markovic, *J. Phys. Chem. Lett.*, 2014, **5**, 14, 2474-2478.
3 L. Tian, J. Wang, K. Wang, H. Wo, X. Wang, W. Zhuang, T. Li and X. Du, *Carbon N. Y.*, 2019, **143**, 457-466.
4 T. Nishi, Y. Hayasaka, T. M. Suzuki, S. Sato, N. Isomura, N. Takahashi, S. Kosaka, T. Nakamura, S. Sato and T. Morikawa, *ChemistrySelect*, 2018, **3**, 17, 4979-4984.
5 L. Negahdar, F. Zeng, S. Palkovits, C. Broicher and R. Palkovits, *ChemElectroChem*, 2019, **6**, 22, 5588-5595.
6 Y. Yi, J. Tornow, E. Willinger, M. G. Willinger, C. Ranjan and R. Schlçgl, *ChemElectroChem*, 2015, **2**, 1929–1937.
7 S. Y. Lim, W. Shen and Z. Gao, *Chem. Soc. Rev.*, 2015, **44**, 362-381.
8 F. D. Kong, S. Zhang, G. P. Yin, J. Liu and Z. Q. Xu, *Int. J. Hydrogen Energy*, 2013, **38**, 22, 9217-9222.
9 J. Durst, C. Simon, F. Hasché and H. A. Gasteiger, *J. Electrochem. Soc.*, 2014, **162**, 1, F190-F203.
10 D. Strmcnik, P. P. Lopes, B. Genorio, V. R. Stamenkovic and N. M. Markovic, *Nano Energy*, 2016, **29**, 29-36.
11 Z. Jiang, Z. J. Jiang, T. Maiyalagan and A. Manthiram, *J. Mater. Chem. A*, 2016, **4**, 5877–5889.
12 Q. Li, S. Tan, L. Li, Y. Lu and Y. He, *Sci. Adv.*, **3**, 7, e1701246.
13 T. V. Vineesh, M. P. Kumar, C. Takahashi, G. Kalita, S. Alwarappan, D. K. Pattanayak and T. N. Narayanan, *Adv. Energy Mater.*, 2015, **5**, 17, 1500658.
14 M. Li, L. Zhang, Q. Xu, J. Niu and Z. Xia, *J. Catal.*, 2014, **314**, 66-72.
15 H. Wang, T. Maiyalagan and X. Wang, *ACS Catal.*, 2012, **2**, 5, 781-794.
16 S. Agnoli and M. Favaro, *J. Mater. Chem. A*, 2016, **4**, 5002-5025.
17 P. Joshi, H. H. Huang, R. Yadav, M. Hara and M. Yoshimura, *Catal. Sci. Technol.*, 2020, **10**, 6599-6610.
18 M. Hara, R. Badam, G. J. Wang, H.-H. Huang and M. Yoshimura, *ECS Trans.*, 2018, **85**, 11, 27-35.
19 H. Tabassum, R. Zou, A. Mahmood, Z. Liang and S. Guo, *J. Mater. Chem. A*, 2016, **4**, 16469–16475.
20 M. Zhang, H. Tao, Y. Liu, C. Yan, S. Hong, J. Masa, A. W. Robertson, S. Liu, J. Qiu and Z. Sun, *ACS Sustain. Chem. Eng.*, 2019, **7**, 3434–3442.
21 H. Mousavi and R. Moradian, *Solid State Sci.*, 2011, 13, **8**, 1459-1464.
22 D. Y. Yeom, W. Jeon, N. D. K. Tu, S. Y. Yeo, S. S. Lee, B. J. Sung, H. Chang, J. A. Lim and H. Kim, *Sci. Rep.*, 2015, **5**, 9817.
23 Y. Zhou, N. Wang, J. Muhammad, D. Wang, Y. Duan, X. Zhang, X.

Dong and Z. Zhang, *Carbon N. Y.*, 2019, **148**, 204-213.
24 S. Wang, L. Zhang, Z. Xia, A. Roy, D. W. Chang, J. B. Baek and L. Dai, *Angew. Chemie - Int. Ed.*, 2012, **51**, 4209–4212.
25 W. Chen, L. Xu, Y. Tian, H. Li and K. Wang, *Carbon N. Y.*, 2018, **137**, 458–466.
26 Y. Zhao, L. Yang, S. Chen, X. Wang, Y. Ma, Q. Wu, Y. Jiang, W. Qian and Z. Hu, *J. Am. Chem. Soc.*, 2013, **135**, 1201–1204.
27 T. Schiros, D. Nordlund, L. Palova, L. Zhao, M. Levendorf, C. Jaye, D. Reichman, J. Park, M. Hybertsen and A. Pasupathy, *ACS Nano*, 2016, **10**, 6574–6584.
28 B. J. Matsoso, K. Ranganathan, B. K. Mutuma, T. Lerotholi, G. Jones and N. J. Coville, *New J. Chem.*, 2017, **41**, 9497-9504.
29 H. Liu, X. H. Zhang, Y. X. Li, X. Li, C. K. Dong, D. Y. Wu, C. C. Tang, S. L. Chou, F. Fang and X. W. Du,*Adv. Energy Mater.*,2020,**10**, 1-7.
30 H. Zhang, L. Xu, Y. Tian, A. Jiao, S. Li, X. Liu, M. Chen and F. Chen, *ACS Omega*, 2019, **4**, 6, 11163-11172.
31 X. Du, C. Du, P. Cai, W. Luo and G. Cheng, *ChemCatChem*, 2016, **8**, 1410–1416.
32 Y. Jin, D. Han, W. Jia, G. Huang, F. Li, X. Chen, R. Li, M. Zheng and W. Gao, *J. Electrochem. Soc.*, 2017, **164**, F638–F644.
33 K. Liao, J. Gao, J. Fan, Y. Mo, Q. Xu and Y. Min, *J. Nanoparticle Res.*, 2017, **19**, 397.
34 K. K. H. De Silva, H. H. Huang and M. Yoshimura, *Appl. Surf. Sci.*, 2018, **447**, 338–346.
35 V. Di Noto, E. Negro, A. Nale, P. J. Kulesza, I. A. Rutkowska, K. Vezzù and G. Pagot, *Electrocatalysis*, 2020, **11**, 143–159.
36 V. Di Noto, E. Negro, K. Vezzú, F. Bertasi and G. Nawn, *Electrochem. Soc. Interface*, 2015, **24**, 2, 59-64.
37 D. Chandra, T. Sato, Y. Tanahashi, R. Takeuchi and M. Yagi, *Energy*, 2019, **173**, 278-289.
38 J. B. Aladekomo and R. H. Bragg, *Carbon N. Y.*, 1990, **28**, 6, 897-906.
39 S. G. Xue, L. Tang, Y. K. Tang, C. X. Li, M. L. Li, J. J. Zhou, W. Chen, F. Zhu and J. Jiang, *ACS Appl. Mater. Interfaces*, 2020, **12**, 4, 4423-4431.
40 J. K. Zak, E. Negro, I. A. Rutkowska, B. Dembinska, V. Di Noto and P. J. Kulesza, in *Encyclopedia of Interfacial Chemistry: Surface Science and Electrochemistry*, Elsevier, Amsterdam, 2018, 651–659.
41 S. Wang, E. Iyyamperumal, A. Roy, Y. Xue, D. Yu and L. Dai, *Angew. Chemie - Int. Ed.*, 2011, **50**, 49, 11756-11760.
42 Y. Zheng, Y. Jiao, L. Ge, M. Jaroniec and S. Z. Qiao, *Angew. Chemie - Int. Ed.*, 2013, **52**, 3110–3116.
43 V. Di Noto, E. Negro, S. Polizzi, F. Agresti and G. A. Giffin, *ChemSusChem* , 2012, **12**, 5, 2451-2459.
44 L. Zhao, X. L. Sui, J. L. Li, J. J. Zhang, L. M. Zhang and Z. B. Wang, *ACS Appl. Mater. Interfaces*, 2016, **8**, 25, 16026–16034.
45 R. Yadav, P. Joshi, M. Hara, T. Yana, S. Hashimoto and M. Yoshimura, *SN Appl. Sci.*, 2020, **2**, 1630.
46 P. Joshi, T. Okada, K. Miyabayashi and M. Miyake, *Anal. Chem.*, 2018, **90**, 10, 6116–6123.
47 S. Jung, C. C. L. McCrory, I. M. Ferrer, J. C. Peters and T. F. Jaramillo, *J. Mater. Chem. A*, 2016, **4**, 3068-3076.
48 H. H. Huang, K. K. H. De Silva, G. R. A. Kumara and M. Yoshimura, *Sci. Rep.*, 2018, **8**, 6849.
49 K. N. Kudin, B. Ozbas, H. C. Schniepp, R. K. Prud'homme, I. A. Aksay and R. Car, *Nano Lett.*, 2008, **8**, 1, 36-41.
50 X. Li, H. Wang, J. T. Robinson, H. Sanchez, G. Diankov and H. Dai, *J. Am. Chem. Soc.*, 2009, **131**, 43, 15939-15944.
51 R. Arenal, A. C. Ferrari, S. Reich, L. Wirtz, J. Y. Mevellec, S. Lefrant, A. Rubio and A. Loiseau, *Nano Lett.*, 2006, **6**, 8, 1812-1816.
52 Q. Cai, D. Scullion, A. Falin, K. Watanabe, T. Taniguchi, Y. Chen, E. J. G. Santos and L. H. Li, *Nanoscale*, 2017, **9**, 3059–3067.
53 L. K. Putri, B. J. Ng, W. J. Ong, H. W. Lee, W. S. Chang and S. P. Chai, *ACS Appl. Mater. Interfaces*, 2017, **9**, 5, 4558-4569.
54 A. Bagri, C. Mattevi, M. Acik, Y. J. Chabal, M. Chhowalla and V. B. Shenoy, *Nat. Chem.*, 2010, **2**, 581-587.
55 Y. Liu, H. Masumoto and T. Goto, *Mater. Trans.*, 2004, **45**, 10, 3023-3027.
56 B. Ertug, in *Sintering Applications*, InTech: Croatia, 2013.
57 Y. R. Luo, *Compr. Handb. Chem. Bond Energies*, 2007, 1–1656.
58 P. Rani and V. K. Jindal, *Appl. Nanosci.*, 2014, **4**, 989-996.
59 N. R. Abdullah, H. O. Rashid, M. T. Kareem, C. S. Tang, A. Manolescu and V. Gudmundsson, *Phys. Lett. Sect. A Gen. At. Solid State Phys.*, 2020, **384**, 12, 126350.
60 V. Pfeifer, T. E. Jones, J. J. Velasco Vélez, R. Arrigo, S. Piccinin, M. Hävecker, A. Knop-Gericke and R. Schlögl, *Chem. Sci.*, 2017, **8**, 2143-2149.
61 V. Pfeifer, T. E. Jones, J. J. Velasco Vélez, C. Massué, M. T. Greiner, R. Arrigo, D. Teschner, F. Girgsdies, M. Scherzer, J. Allan, M. Hashagen, G. Weinberg, S. Piccinin, M. Hävecker, A. Knop-Gericke and R. Schlögl, *Phys. Chem. Chem. Phys.*, 2016, **18**, 2292–2296.
62 J. C. Meier, C. Galeano, I. Katsounaros, A. A. Topalov, A. Kostka, F. Schüth and K. J. J. Mayrhofer, *ACS Catal.*, 2012, **2**, 5, 832-843.
63 I. C. Man, H. Y. Su, F. Calle-Vallejo, H. A. Hansen, J. I. Martínez, N. G. Inoglu, J. Kitchin, T. F. Jaramillo, J. K. Nørskov and J. Rossmeisl, *ChemCatChem*, 2011, **3**, 7, 1159-1165.
64 N. T. Suen, S. F. Hung, Q. Quan, N. Zhang, Y. J. Xu and H. M. Chen, *Chem. Soc. Rev.*, 2017, **46**, 337–365.
65 X. Lu, W. L. Yim, B. H. R. Suryanto and C. Zhao, *J. Am. Chem. Soc.*, 2015, **137**, 8, 2901-2907.
66 G. L. Tian, M. Q. Zhao, D. Yu, X. Y. Kong, J. Q. Huang, Q. Zhang and F. Wei, *Small*, 2014, **10**, 11, 2251-2259.
67 J. Tian, Q. Liu, A. M. Asiri, K. A. Alamry and X. Sun, *ChemSusChem*, 2014, **7**, 8, 2125-2130.
68 T. Y. Ma, S. Dai, M. Jaroniec and S. Z. Qiao, *Angew. Chemie - Int. Ed.*, 2014, **53**, 28, 7281-7285.
69 T. Shinagawa, A. T. Garcia-Esparza and K. Takanabe, *Sci. Rep.*, 2015, **5**, 13801.
70 T. Reier, D. Teschner, T. Lunkenbein, A. Bergmann, S. Selve, R. Kraehnert, R. Schlögl and P. Strasser, *J. Electrochem. Soc.*, 2014, **161**, 9, F876-F882.
71 L. B. Boinovich, A. M. Emelyanenko, A. S. Pashinin, C. H. Lee, J. Drelich and Y. K. Yap, *Langmuir*, 2012, **28**, 2, 1206–1216.
72 D. Sen, R. Thapa and K. K. Chattopadhyay, *ChemPhysChem*, 2014, **15**, 12, 2542-2549.
73 Y. Shao, G. Yin and Y. Gao, *J. Power Sources*, 2007, **171**, 2, 558-566.
74 K. H. Lim, H. S. Oh, S. E. Jang, Y. J. Ko, H. J. Kim and H. Kim, *J. Power Sources*, 2009, **193**, 2, 575-579.
75 S. E. Jang and H. Kim, *J. Am. Chem. Soc.*, 2010, **132**, 42, 14700–14701.
76 E. A. Il'inchik, V. V. Volkov and L. N. Mazalov, *J. Struct. Chem.*,

2005, **46**, 523-534.

77 S. Chen, D. Z. Wang, J. Y. Huang and Z. F. Ren, *Appl. Phys. A Mater. Sci. Process.*, 2004, **79**, 1757-1759.

78 A. Sinha, T. Mahata and B. P. Sharma, *J. Nucl. Mater.*, 2002, **301**, 2-3, 165-169.

79 J. A. Bigdeloo and A. M. Hadian, *Int. J. Recent Trends Eng,* 2009, **1**, 5, 176-180.